Confinement-Shear Lattice Model for Concrete Damage in Tension and Compression: II. Computation and Validation

Gianluca Cusatis[1]; Zdeněk P. Bažant, F.ASCE[2]; and Luigi Cedolin, M.ASCE[3]

Abstract: The concrete material model developed in the preceding Part I of this study is formulated numerically. The new model is then verified by comparisons with experimental data for compressive and tensile uniaxial tests, biaxial tests, and triaxial tests, as well as notched tests of mode I fracture and size effect.

DOI: 10.1061/(ASCE)0733-9399(2003)129:12(1449)

CE Database subject headings: Concrete; Microstructure; Fractures; Damage; Softening; Failures; Materials tests; Computer analysis; Nonlinear analysis; Particle interactions; Particle distribution.

Introduction

In Part I of this study, a new three-dimensional constitutive model for concrete has been formulated as a three-dimensional lattice connecting the centers of randomly distributed aggregate particles. In the present Part II, a numerical algorithm for this model will be presented and the model will be validated by comparing numerical results and experimental data found in the literature for typical uniaxial, biaxial, and triaxial tests, as well as notched tests of model I fracture and size effect. Only short-time loading, for which creep is unimportant, and loading rates low enough for dynamic effects to be absent, will be considered. All the definitions and notations from part I will be retained.

Numerical Implementation and Stability Conditions

Concrete is here idealized as an assembly of particles whose interaction can be described by a two-node finite element (Cusatis et al. 2003). Like the finite element method in general, this leads to the following matrix equation of motion for the structure:

$$\mathbf{M}\ddot{\mathbf{Q}}+\mathbf{C}\dot{\mathbf{Q}}+\mathbf{P}(\mathbf{Q})=\mathbf{F}(t) \tag{1}$$

Here $\mathbf{M}$=mass matrix of components M_i; $\mathbf{P}$=vector of internal forces of components P_i, which are obtained by assembling the contributions from all the finite elements (all struts); $\mathbf{Q}$=the vector of kinematic variables Q_i (displacements and rotations of all aggregates); $\mathbf{F}(t)$=given load history; and subscripts $i=1,2,...,N$ number the generalized displacement components. The damping matrix $\mathbf{C}$, of components C_i, is introduced only for the sake of generality and is assumed zero in computations.

Eq. (1) can be integrated explicitly or implicitly. The implicit methods allow much larger time steps but require considerably more computational effort per time step than the explicit methods. The explicit methods have severe limitations on the time step length because of the condition of numerical stability, but have the advantage of much smaller memory requirements. In the present three-dimensional numerical simulations, there are thousands of unknowns even for the smallest test specimen, and so computer memory limitations and running time are important. Therefore, the explicit method, based on a central difference algorithm, is selected (it allowed running all the present problems on a personal computer with a 750 MHz Pentium III processor). The central difference approximation of (1) is

$$\dot{Q}_i^{n+1/2}=a\dot{Q}_i^{n-1/2}+b(P_i^n-F_i^n)/M_i \tag{2}$$

for unconstrained degrees of freedom and

$$\dot{Q}_i^{n+1/2}=\dot{\delta}_i^{n+1/2}=\dot{\delta}_i(t^{n+1/2}),\quad R_i^n=P_i^n+M_i(\dot{\delta}_i^{n+1/2}-a\dot{\delta}_i^{n-1/2})/b \tag{3}$$

for constrained degrees of freedom (see the Appendix); $\dot{\delta}_i(t)$=prescribed velocity history for the ith degree of freedom; R_i^n=work-conjugate reaction of the constraint; $n=1,2,...,M$ are the labels for discrete times t_n subdividing time t into intervals Δt. The parameter values are: $a=0$, $b=\Delta t/2$ for $n=0$, and $a=(1-v)/(1+v)$, $b=\Delta t/(1+v)$ for $n>0$, where $v=C\Delta t/2$, Δt=time step, C=damping coefficient, and $\mathbf{C}=C\mathbf{M}$ (which was considered as zero in all calculations).

The numerical stability condition simply is $\Delta t<2/\omega$ (Belytschko et al. 2000), where ω represents the highest natural frequency of the system (Bažant and Cedolin 1991). Because the longitudinal displacement field throughout the element is linear, the frequency of free vibrations in the longitudinal direction is $\omega_N^2=4E_N/(\rho l^2)$ (Belytschko et al. 2000).

For the shear free modes, a similar formula can be derived. In two dimensions (the extension to three dimensions being straightforward) the kinetic energy associated with the shear deformation of the element is

[1]Graduate Student, Dept. of Structural Engineering, Technical Univ. (Politecnico) of Milan, Milan 20133, Italy. E-mail: cusatis@stru.polimi.it

[2]McCormick School Professor and W. P. Murphy Professor of Civil Engineering and Materials Science, Northwestern Univ., Evanston, IL 60208. E-mail: z-bazant@northwestern.edu

[3]Professor of Structural Engineering, Dept. of Structural Engineering, Technical Univ. (Politecnico) of Milan, Milan 20133, Italy. E-mail: cedolin@stru.polimi.it

Note. Associate Editor: Stein Sture. Discussion open until May 1, 2004. Separate discussions must be submitted for individual papers. To extend the closing date by one month, a written request must be filed with the ASCE Managing Editor. The manuscript for this paper was submitted for review and possible publication on August 26, 2002; approved on February 21, 2003. This paper is part of the ***Journal of Engineering Mechanics***, Vol. 129, No. 12, December 1, 2003. ©ASCE, ISSN 0733-9399/2003/12-1449–1458/$18.00.

$$\mathcal{K}_T=\frac{1}{2}\int_0^{l_1}\rho A[\dot{v}(x_1)]^2dx_1+\frac{1}{2}\int_0^{l_2}\rho A[\dot{v}(x_2)]^2dx_2 \qquad (4)$$

where $v(x_1)$ and $v(x_2)$=transversal velocities of particles 1 and 2, respectively; $v(x_1)=v_1+x_1\vartheta_1$, $v(x_2)=v_2+x_2\vartheta_2$, and $\dot{v}(x_1)=\dot{v}_1+x_1\dot{\vartheta}_1$, $\dot{v}(x_2)=\dot{v}_2+x_2\dot{\vartheta}_2$ (Cusatis et al. 2003). By substituting these expressions into Eq. (4), we get $\mathcal{K}_T=\dot{\mathbf{q}}^T\mathbf{M}_T^c\dot{\mathbf{q}}/2$, where $\dot{\mathbf{q}}^T=\{\dot{v}_1,\dot{\vartheta}_1,\dot{v}_2,\dot{\vartheta}_1\}$ and

$$\mathbf{M}_T^c=\rho A\begin{bmatrix} l_1 & l_1^2/2 & 0 & 0 \\ l_1^2/2 & l_1^3/3 & 0 & 0 \\ 0 & 0 & l_2 & -l_2^2/2 \\ 0 & 0 & -l_2^2/2 & l_2^3/3 \end{bmatrix} \qquad (5)$$

The lumped mass matrix can be obtained by simply neglecting the terms out of the diagonal, as usually done for beam elements (Belytschko et al. 2000); $\mathbf{M}_T=\rho A\ \mathrm{diag}[l_1,l_1^3/3,l_2,l_2^3/3]$. The elastic energy associated with these free modes can be expressed as $\mathcal{W}_T=\int_0^l AE_T\varepsilon_T^2dx/2$. Since the shear strain is $\varepsilon_T=(v_2-v_1-l_2\vartheta_2-l_1\vartheta_1)/l$ (Cusatis et al. 2003) one gets $\mathcal{W}_T=\mathbf{q}^T\mathbf{K}_T\mathbf{q}/2$, where $\mathbf{q}^T=\{v_1,\vartheta_1,v_2,\vartheta_1\}$ and

$$\mathbf{K}_T=\frac{AE_T}{l}\begin{bmatrix} 1 & l_1 & -1 & l_2 \\ l_1 & l_1^2 & -l_1 & l_1l_2 \\ -1 & -l_1 & 1 & -l_2 \\ l_2 & l_1l_2 & -l_2 & l_2^2 \end{bmatrix} \qquad (6)$$

The frequency of free vibrations in the transversal direction is the eigenvalue of the following eigenvalue problem $\det(\mathbf{K}_T-\omega_T^2\mathbf{M}_T)=0$ which, with the notations $l_1=c_1l$ and $l_2=c_2l$, becomes $-c_1E_T-c_1E_T/3-c_2E_T-c_2E_T/3+c_1c_2l^2\rho\omega_T^2/3=0$. Since $c_1+c_2=1$ and $E_T=\alpha E_N$, the last equation gives $\omega_T^2=\alpha\omega_N^2/(c_1c_2)$. Numerical stability is determined by the highest frequency of the system, $\omega_{\max}$, which is bounded from above by the maximum unconstrained element frequency present in the mesh. Consequently, $\omega_{\max}^2<\chi\omega_N^2$, where $\chi=\max[1,\alpha/(c_1c_2)]$. Since $\alpha=0.25$, as we will see later on, we have $\chi=\max[1,(4c_1c_2)^{-1}]$. One may check that $(4c_1c_2)^{-1}\geqslant 1$ for any c_1 and c_2 (with $c_1+c_2=1$), and so the maximum frequency is given by the shear behavior. So, the stability condition is $\Delta t\leqslant 2/\omega_{\max}=l/(c_N\sqrt{\chi})$, where $c_N=\sqrt{E_N/\rho}$ is the longitudinal wave speed in the connecting strut.

Although the foregoing stability analysis strictly applies only to linear systems, it also provides useful numerical stability estimates for nonlinear problems. Material and geometric nonlinearities generally do not destabilize the numerical algorithm (Belytschko et al. 2000). In any case, it is important to check the energy balance during the computation: any significant loss in energy balance (5% or more) indicates a numerical instability or bifurcation. Energy balance checks are particularly important for nonlinear constitutive relations, since a temporary instability can often be arrested by material dissipation or a bifurcation missed, hiding completely erroneous results.

Identification of Material Properties and Model Parameters

The parameters of the model have been calibrated by fitting the response of concrete in uniaxial compression reported in van Vliet and van Mier (1995). Comparisons with other experimental data relevant to different kinds of tests are conducted without changing the values of the parameters. These comparisons are only qualitative, intended to demonstrate that one set of parameters is capable of modeling all the most important types of experiments.

The reference properties of concrete are the following: cement content $c=375\ \mathrm{kg/m^3}$, water–cement ratio $w/c=0.5$, aggregate–cement ratio $a/c=4.8$, maximum aggregate size $d_a=8$ mm; the granulometric distribution: 15, 10, and 5% in mass of aggregates with characteristic sizes of 8, 6.5, and 5 mm, respectively. The optimized parameters defining the constitutive law (see Cusatis et al. 2003) are $\alpha=0.25$, normal elastic modulus of cement mortar $E_c=50{,}000$ MPa, normal elastic modulus of aggregate $E_a=6E_c$, tensile mesostrength (strength at mesolevel of microstructure) $\sigma_t=13.5$ MPa, fracture energy at the mesolevel (with confining effect) $G_t=0.28$ N/mm, $\hat{a}=4.5\ \mathrm{MPa^{-1}}$, mesocohesion $\sigma_s=2\sigma_t$, compressive mesostrength $\sigma_c=16\sigma_t$, hardening parameter at the mesolevel $K_c=0.26E_c$, shape parameter of compression cap $\beta=1$, and slope of the hyperbola asymptote $\mu=0.2$, $n_t=n_c=2$.

Response to Compressive Uniaxial Stress

The specimens are prisms with a constant cross section of $100\times100\ \mathrm{mm^2}$ and two different heights: 100 and 200 mm. Fig. 1(a) shows the generated aggregate distribution for the smaller specimen and Fig. 1(b) shows the corresponding lattice. The total number of particles is 1,492 for the 100 mm specimen and 2,892 for the 200 mm specimen. The two lattices consist of 10,878 and 21,405 elements, respectively.

In the experiment, the load is applied under displacement control by a loading device that does not allow rotations of the loading platens during the tests. The tests are performed in two ways: with untreated loading platens, which develop considerable friction, and with platens covered by two friction-reducing Teflon sheets of thickness of 0.1 mm each, with a grease layer of 0.05 mm between the sheets. To simulate these two conditions, a simplified frictional boundary is used. The nodes at which boundary conditions are imposed are first considered as constrained in the directions X, Y orthogonal to the applied load. Through Eq. (3), the reactions R_{IX}, R_{IY}, and R_{IZ} are computed at each node. If the total shear force $R_{IT}=\sqrt{R_{IX}^2+R_{IY}^2}$ is greater than μ_pR_{IZ}, the constraint is released, and by imposing $F_{IT}=\mu_pR_{IZ}$, the velocities are computed from Eq. (2). Here, μ_p is the coefficient of friction, the value of which has been assumed equal to 0.3 for untreated steel platens and to 0.02 for the platen with Teflon sheets. As pointed out by van Mier et al. (1997), the coefficient of friction can actually vary during the test. Vonk (1992) estimated that, for Teflon sheets, $\mu_p\approx0.03$ before the peak of the load–displacement curve and $\mu_p\approx0.01$ during the descending branch. Nevertheless, due to lack of information, constant values of μ_p are assumed in the simulations that follow.

To determine Young's modulus $\overline{E}$ and the (macroscopic) Poisson's ratio $\overline{\nu}$ of the equivalent (smeared, homogenized) elastic continuum, the response of the specimens under small loads corresponding to macroscopically uniform stress and strain is computed. The Young's modulus is calculated from the average axial strain $\varepsilon_Z=\delta_Z/L_Z$ and average axial stress $\sigma_Z=R_Z/(L_XL_Y)$, where δ_Z is the relative displacement applied at the ends of the specimen, R_Z is the computed overall reaction, and L_X, L_Y, and L_Z are the dimensions of the specimen. This calculation yields $E=22{,}900$ MPa.

Poisson's ratio is calculated by the following procedure (Bažant et al. 1990). For each node within an interior region of the

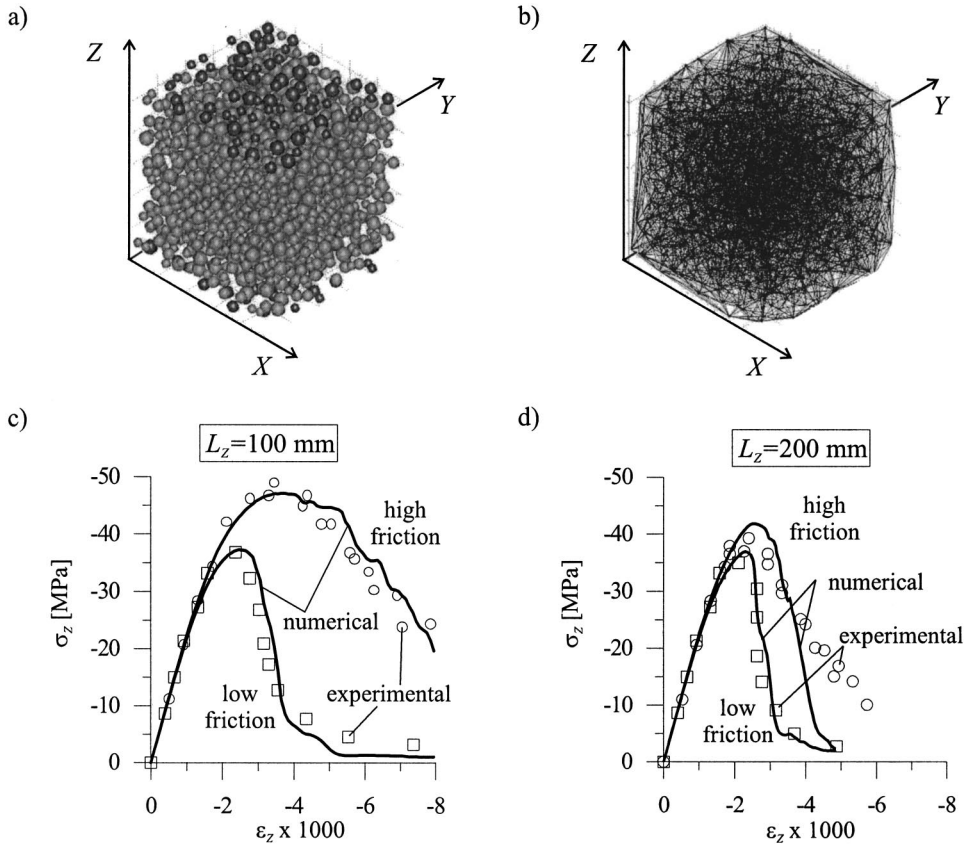

Fig. 1. (a) Generated aggregate distribution; (b) corresponding mesh; (c) effect of friction for a 100-mm-long specimen; and (d) effect of friction for a 200-mm-long specimen

specimen (not influenced by the boundary conditions), the displacements in the longitudinal Z direction and transversal X and Y directions are plotted as functions of the corresponding spatial coordinate. The slope of the regression lines of the three plots represents the macroscopic equivalent strains ε_X, ε_Y, and ε_Z. By the equations $\overline{\nu}_X = -\varepsilon_X/\varepsilon_Z$ and $\overline{\nu}_Y = -\varepsilon_Y/\varepsilon_Z$ the macroscopic Poisson's ratios in the X and Y directions can be computed. For $\sigma_Z = -2.9$ MPa one gets $\overline{\nu}_X = 2.206\times10^{-5}/1.159\times10^{-4} = 0.1904$ and $\overline{\nu}_Y = 2.186\times10^{-5}/1.159\times10^{-4} = 0.1887$, which are in the range of the usual Poisson's ratios for concrete. Numerical experiments have shown that the value of the macroscopic Poisson's ratio depends only on the ratio between the shear elastic stiffness and the normal elastic stiffness at the mesolevel, i.e., the parameter α (Cusatis et al. 2003). The elastic properties can be calibrated in two steps. First, parameter α is set so as to match the given macroscopic Poisson ratio. Second, the elastic stiffness E_N for the normal components of the connections is optimized in order to match the required macroscopic Young's modulus.

Consider now the inelastic response in the tests of van Vliet and van Mier (1995). In Figs. 1(c and d), each computed curve is the average of six curves obtained by computing the response of six specimens with different generated mesostructures. The coefficient of variation of the peak average stress is $\omega_c = 1.1\%$. Fig. 1(c) shows the effect of friction between the specimen ends and the loading platens for a 100-mm-long specimen, and Fig. 1(d) shows the same effect for a 200-mm-long specimen.

The computations agree with the well-known experimental facts about friction. The magnitude of the frictional stresses at the end of the specimens significantly influences both the peak stress and the post peak slope of the load–deflection curve. The higher the friction, the higher is the peak stress and the lower is the slope of the softening curve after the peak. The difference is more pronounced for the shorter (bulkier) specimens than for the longer (slenderer) ones in which the central part is virtually uninfluenced by the end restraint. As seen in Figs. 2(a and b) (for the 200-mm-long specimen) and in Figs. 2(c and d) (for the 100-mm-long specimen), when a friction reducing material is used, the computed failure occurs through a longitudinal splitting crack. Otherwise, concrete spalls at the midlength of the specimen and the well-known pyramids shear off at the specimen ends. Figs. 2(a–d) also document that the damage localizes during failure. This confirms that the nominal stress–strain curve cannot be regarded as a macroscopic material property. The agreement between the numerical and experimental results is satisfactory. This proves the intrinsic capability of the model to capture damage localization which occurs during failure. As expected, this capability can arise only from the randomness and discreteness of the mesostructure and is unattainable by the constitutive relation alone.

Fig. 3(a) presents the normalized longitudinal stress as a function of the relative volume change $\Delta V/V_0 = \varepsilon_X + \varepsilon_Y + \varepsilon_Z$. The numerical results are qualitatively compared with the experimental data by Kupfer et al. (1969). They show a decrease of the volume of the specimen proportional to the applied stress up to about 30% of the peak stress. After that, the simulated stress–strain relation becomes nonlinear and the rate of volume decrease tends to diminish. The minimum computed volume is observed at about 70% of the peak load. If the uniaxial applied stress magnitude is increased further, the specimen starts to expand. At a certain moment $\Delta V/V_0$ becomes positive. The experimental behavior is similar although the loss of linearity and the minimum

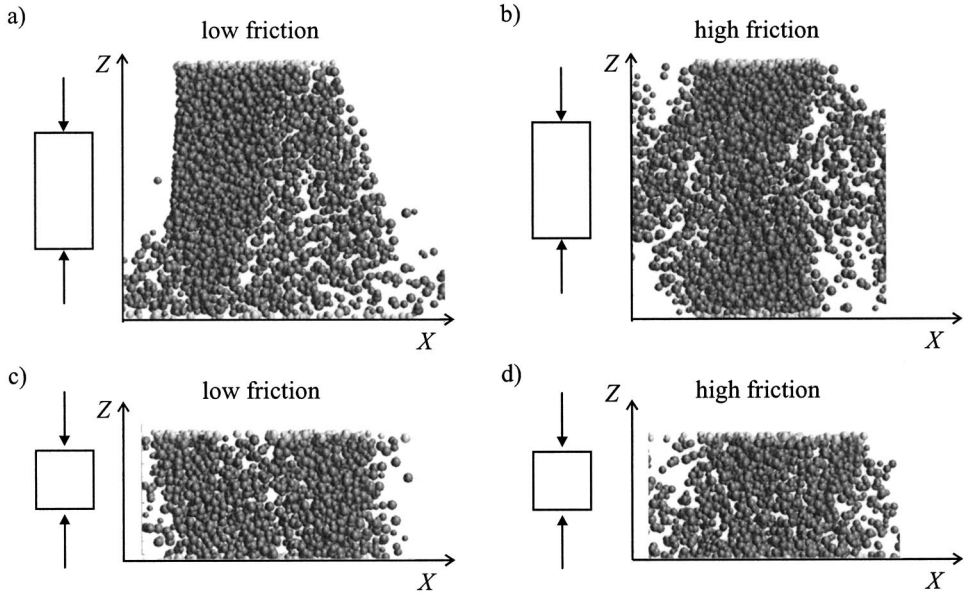

Fig. 2. Amplified deformed shapes at failure: (a) for the 100-mm-long specimen and $\mu_p = 0.02$; (b) for the 100-mm-long specimen and $\mu_p = 0.3$; (c) for the 200-mm-long specimen and $\mu_p = 0.02$; and (d) for the 200-mm-long specimen and $\mu_p = 0.3$

volume are observed at higher load levels (about 50 and 95% of the strength, respectively). The volumetric expansion predicted by the present model for uniaxial compression appears to be larger than that seen in experiments. Nevertheless, note that numerical computation of the volume changes takes into account also the effect of all localized failures happening on the specimen surface (e.g., small aggregates located close to the surface spalled out during failure). These failures are not normally included in the experimental data since the measurements are taken from surface points at which no localized failure occurs (thanks to a glue or a clamping force).

The nonlinear lateral expansion under high compressive stress can also be characterized in terms of the equivalent Poisson's ratio, computed by the same regression procedure as explained for the elastic regime. Fig. 3(b) shows the plots of the equivalent Poisson's ratios in directions X and Y and of their mean values as functions of the applied stress. Before the peak, the computed values in the two directions are almost identical, which confirms the isotropy of macroscopic behavior of concrete. After the peak, due to random failure localization, the isotropy gets lost and the measured Poisson's ratios become quite different. At the peak load, the equivalent Poisson's ratio is 0.5, which agrees with the value reported by van Mier (1986).

The ability of the model to predict cyclic behavior under uniaxial compressive stress is checked through the analysis of concrete specimens on which unloading–reloading cycles are performed in the softening range of the stress–strain curve. As shown by Fig. 3(c), the model is able to reproduce the progressive decrease of stiffness and the widening of the hysteresis loops with increasing number of cycles. The bent shape of the computed hysteresis loops is also very similar to the usual experimental shape (see, e.g., Sinha et al. 1964).

One debated question has been whether the consecutive peaks end up on a unique envelope, the same as the softening curve for monotonic loading. This property, if true, would not only simplify modeling but also would enable replacing the tests of postpeak softening with the cyclic tests which are easier. In literature, one can find conflicting experimental results; for example Sinha et al. (1964) find the postpeak stress–strain envelope to be unique while Hognestad et al. (1955) make the opposite conclusion. To illuminate this question, the computed monotonic curve (dashed line) is also plotted in Fig. 3(c) for the same specimen (with the same random mesostructure) as used for the cyclic test simulations. These numerical results indicate that the hypothesis of a unique postpeak stress–strain envelope at the macroscopic level is, strictly speaking, invalid. However, the departure from the monotonic curve is small, in fact smaller than the usual scatter of the experimental postpeak curves in compression. The large scatter probably explains why the experimental information on the uniqueness of envelope is ambiguous.

Response to Tensile Uniaxial Stress

The calculations of the response to tensile uniaxial stress use the same concrete mix design and model parameters as optimized in the preceding section. Fig. 4(a) shows the geometry of a typical specimen used to compute the macroscopic tensile strength. The thickness is assumed equal to $4\,d_a = 32$ mm. The load is applied, as usual in experiments, under displacement control, and the loading platens are allowed to rotate freely. Fig. 4(c) shows the computed nominal stress–strain curves for six specimens with different randomly generated mesostructures. The stress σ_Z shown is computed under the assumption that the applied load P is uniformly distributed over the cross-section area at the midlength of the specimen and that the strain ε_Z is the average of the displacements measured across the crack based over the base of $L_m = 50$ mm. The mean value of the peak stresses is $f'_t = 4.264$ MPa and their coefficient of variation is $\omega_t = 2.22\%$. It is noteworthy that the value f'_t is about 10% of the compressive strength f'_c (assumed as the peak stress of the stress–strain curve of the 200-mm-long specimen with untreated platens). This property, which agrees with the experimental evidence, was far from achievable with the previous random discrete microstructural

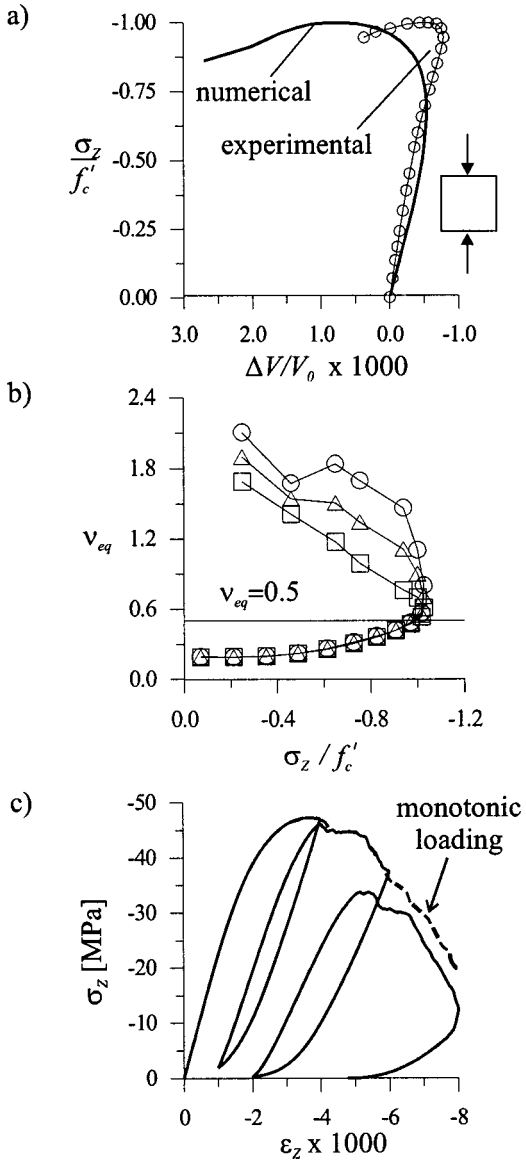

Fig. 3. (a) Volumetric expansion under uniaxial compression; (b) equivalent Poisson's ratio as a function of the applied stress; and (c) cyclic behavior under uniaxial compression

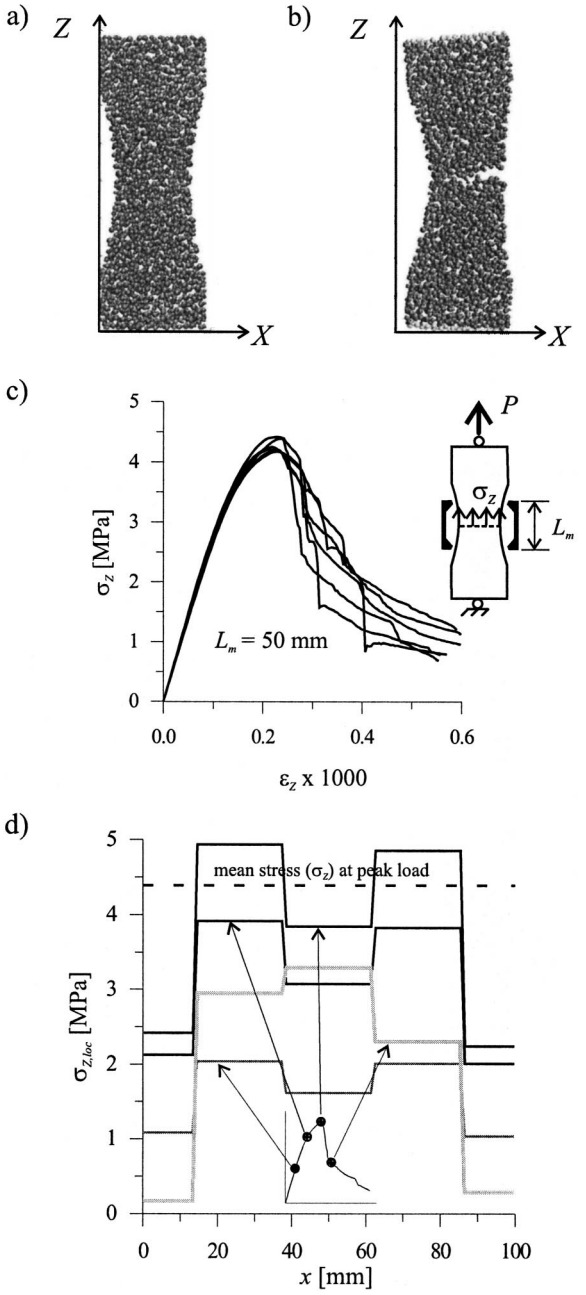

Fig. 4. (a) Typical specimen used for uniaxial tension tests; (b) typical deformed (amplified) shape at failure under tension; (c) numerical stress-strain curves obtained in tension; and (d) typical evolution of the averaged stress profiles at the midlength of the specimen under tension

models. Fig. 4(b) shows a typical failure mode which, as proven by many experimental studies (Cedolin et al. 1987), is asymmetric. The specimen fails by a crack propagating from one side of the specimen to the other. To clarify the asymmetric nature of the failure it is useful to plot the evolution of the stress profiles at the midlength of the specimen [Fig. 4(d)]. These profiles are obtained by averaging the interparticle forces over a representative volume of material whose dimension is assumed to be three times the maximum aggregate size ($3\,d_a = 3 \times 8$ mm $= 24$ mm). The stress distribution over the cross section of the specimen is not homogeneous and not symmetric, and the asymmetry is seen to increase as inelastic deformation progresses. The direct consequence of this fact is that the average stress at peak load (usually referred to as the tensile strength) is substantially lower than the actual tensile strength of the material. Exactly the same conclusion has been drawn by Cedolin et al. (1987) by analyzing a concrete specimen in direct tension through optical interferometry with laser light.

To complete the analysis of the tensile response, we must consider the response under tensile cyclic loads. Figs. 5(a–c) show the response for three types of unloading rule from the postpeak portion of the nominal stress–strain relation obtained by loading double-notched specimens. The tensile load is decreased to a lower value in Fig. 5(a), and to almost zero in Fig. 5(b). The load is reversed from tension to compression in Fig. 5(c). The computed curves share with the typical experimental data (e.g., Reinhardt and Cornellissen 1984) several features. The loading and unloading stiffnesses decrease after each cycle while the area within the hysteretic loop increases. In contrast to what is found

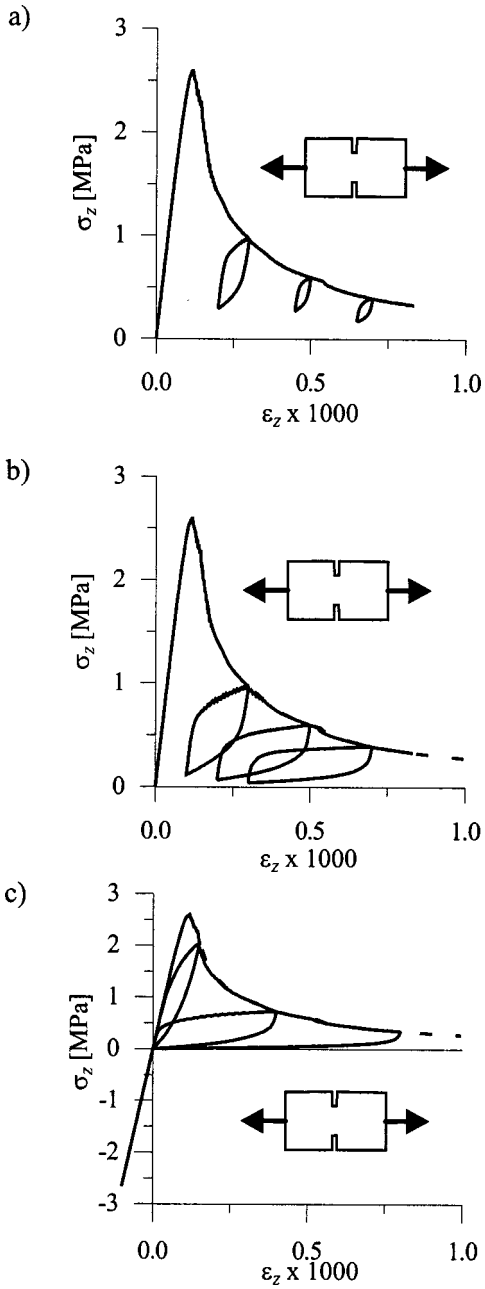

Fig. 5. Cyclic behavior under tension: (a) unloading to a lower tensile stress; (b) unloading to almost zero stress; and (c) unloading to compressive stress

for compression, the peak stress for tension after reloading lies exactly on the curve obtained for monotonic loading. This is probably due to the fact that the damage in tension is much more localized and thus locally more severe. The numerical and experimental results for the irreversible strain component differ. The experiments show this component to increase after each cycle whereas the numerical simulations always indicate unloading to the origin, i.e., the irreversible strain is zero.

Fracture and Size Effect

Let us now consider the nonlinear fracture behavior of concrete which leads to the well-known *size effect* on the nominal strength of the concrete structures (Bažant 2002a,b). Knowledge of the size effect in turn allows identification of the macroscopic fracture properties and characteristic length of the heterogeneous brittle material as well as calibration of the microstructural model.

For a long time, the size effect was explained statistically—as a consequence of the randomness of material strength. Various limited experimental data on the size effect were interpreted in terms of Weibull weakest-link theory (e.g., Mihashi and Izumi 1977). Beginning with Bažant (1984) it was shown that whenever failure does not occur at the initiation of cracking, the mean size effect must properly be explained deterministically—by stress redistribution, with the inherent energy release, caused by growth of a large fracture or a large fracture process zone on the macroscale, and that the randomness of material strength plays only a negligible role in the mean response (of course, it still controls the variance of response). By such reasoning, and using nonlinear fracture mechanics, a size effect law was proposed (Bažant 1984) to describe a smooth transition between the asymptotic cases of plastic limit analysis of zero-size structures (for which there is no size effect) and the linear elastic fracture mechanics of infinite-size structures (for which the size effect is the strongest possible).

To check the size effect given by the present model, we now analyze the response of geometrically similar notched specimens [whose geometry is shown in Fig. 6(a)] loaded in fracture mode I. The platens are considered to rotate freely. For each size, six specimens have been analyzed. The responses of the specimens with the smallest size have been also used to compute the total fracture energy G_F from the so-called *work of fracture*, which is the total energy dissipated by fracture during the test. G_F can be computed by integrating the area under the complete nominal stress–strain curve in Fig. 6(b); $G_F = L\int_0^\infty \sigma_n(\varepsilon_n)d\varepsilon_n$. The nominal stress and strain are defined as $\sigma_n = P/bD$ and $\varepsilon_n = \Delta u/L$, where Δu is the relative displacement between loading platens, with $L = 8D/3$. The mean value of the total fracture energy is $G_F = 85.07$ N/m and its coefficient of variation is $\omega_F = 19.96\%$. This G_f value is in agreement with the usual fracture energy reported in the literature for the assumed concrete mix-design (e.g., Cedolin et al. 1987).

Based on the computed peak stresses σ_{nu} for the three sizes considered, the size effect law (SEL) proposed by Bažant (1984), $\sigma_{nu} = \sigma_0(1 + D/D_0)^{-1/2}$ (where σ_0, D_0=constants, D=characteristic structure size), can be identified by the following linear regression. In the plot of $Y = 1/\sigma_{nu}^2$ versus $X = D$, the SEL appears as a straight line $Y = AX + C$, and $\sigma_0 = 1/\sqrt{C}$, $D_0 = C/A$. The coefficients A and C can be determined by performing a linear regression of Y versus X. We get $A = 1.028\times10^{-3}$ MPa^{-2}/mm and $C = 5.7\times10^{-2}$ MPa^{-2} from which $\sigma_0 = 4.18$ MPa and $D_0 = 55.75$ mm. Fig. 6(c) shows the computed peak stresses, their mean values, and the identified SEL. Note that the three mean values of the peak stresses lie on the straight line $Y = AX + C$ almost exactly, which proves that the average behavior of the present model matches Bažant's size effect law very well. After determining A and C by linear regression, one can get the fracture energy G_f as $G_f = \sigma_0^2 D_0 g(\alpha_0)/E$ where $g(\alpha)$ is the dimensionless LEFM energy release function, $\alpha_0 = a_0/D$ and a_0 is the length of the notch (see Bažant and Planas 1998). The fracture energy G_f is known to coincide with the area under the initial tangent of the softening stress-separation curve (cohesive law) at the macroscopic level; as shown by Planas et al. (1992) (see also Bažant and Planas 1998) and demonstrated in detail by Bažant and Yu (2002) by comparing size effect analysis with an accurate cohesive crack propagation analysis. For the present geometry (e.g., Broek 1988), $g(\alpha)$

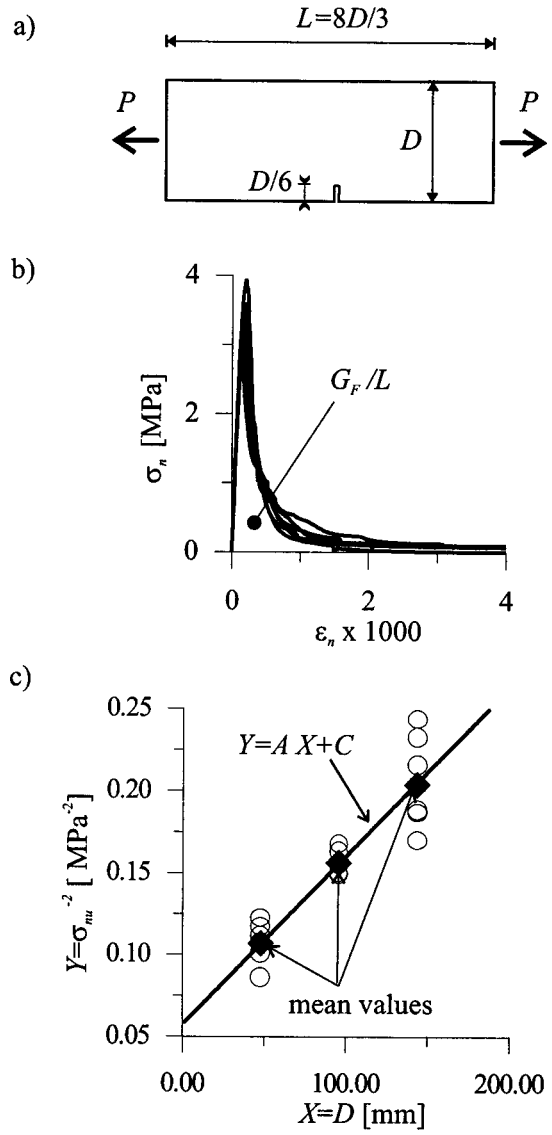

Fig. 6. (a) Geometry of similar specimens used for the size effect analysis; (b) nominal stress-nominal strain complete curve for the smallest specimen size; and (c) linear regression identifying the parameters of the Bažant's size effect law

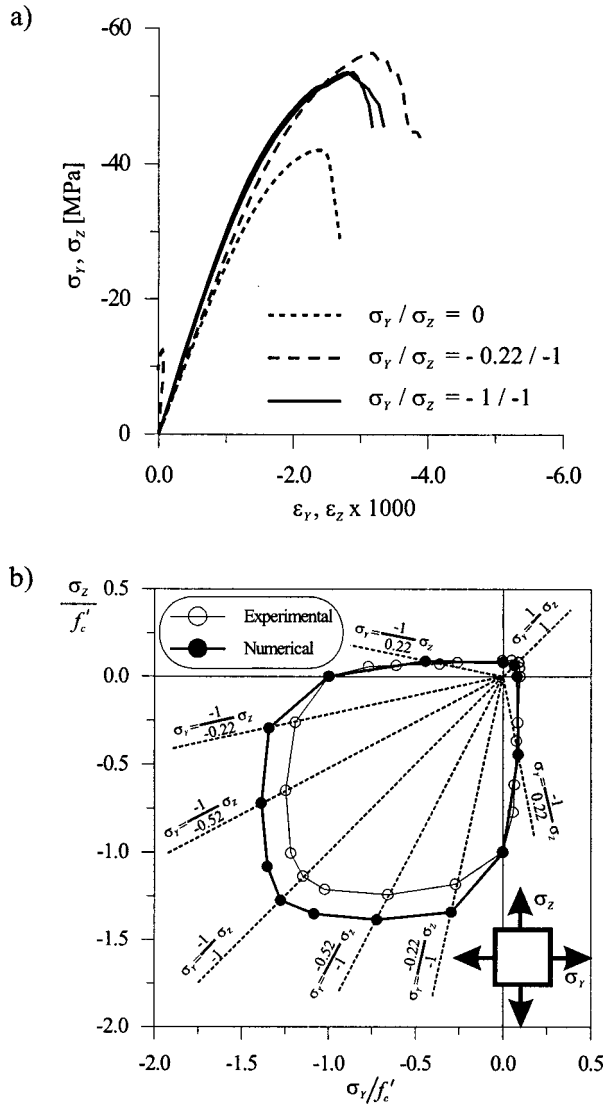

Fig. 7. (a) Numerical stress–strain curves obtained in biaxial compression and (b) comparison between numerical and experimental failure envelopes for biaxial loading

$=\alpha\pi(1.12-0.23\alpha+10.56\alpha^2-21.74\alpha^3+30.42\alpha^4)^2$. Since $\alpha_0=1/6$, we get $G_f=37.45$ N/m. From the statistics of the regression analysis, we can further compute an approximate coefficient of variation of G_f, which is $\omega_f=10.7\%$. The computations yield the ratio

$$G_F/G_f=2.3 \tag{7}$$

which is very close to the value 2.5 estimated by Planas et al. (1992), derived by Bažant and Yu (2001), and further supported by extensive statistical analysis of the experimental data from literature (Bažant and Becq-Giraudon 2002); for further discussion, see Bažant (2002a,b).

From the SEL we can also compute the effective length of the asymptotic fracture process zone, $c_f=D_0g(\alpha_0)/g'(\alpha_0)=6.095$ mm, and its coefficient of variation $\omega_{cf}=30.26\%$.

Biaxial and Triaxial Response

Consider now the simulation of biaxial stress states. Concrete specimens 200 mm×200 mm×50 mm are subjected to compression, biaxial compression–tension, and biaxial tension. Usually, the load is applied by means of brush bearing platens in order to minimize the effect of friction, which is not specifically modeled in the present simulations. The loading paths in the space of principal stresses σ_Y and σ_Z are proportional, i.e., $k=\sigma_Z/\sigma_Y=$constant. Fig. 7(a) shows the computed nominal stress–strain curves for three values of the load ratio, $k=0$, 0.22, and 1, in biaxial compression. They are the same as in the tests of Kupfer et al. (1969). Fig. 7(b) shows the experimental (Kupfer et al. 1969) and numerical failure envelopes which are constructed from the peak stresses for various values of k, normalized by the uniaxial compressive strength. The numerical results fit the experimental data satisfactorily. In biaxial compression, the strength of concrete increases with k and reaches its maximum for $k\approx0.5$, although the postpeak behavior is always softening.

In triaxial tests with sufficient minimum magnitude of the compressive stress, softening of concrete reverses to hardening. Fig. 8(a) shows a comparison between the numerical results for hydrostatic compression tests and the experimental data by Green and Swanson (1973). The tests are carried out by applying on the

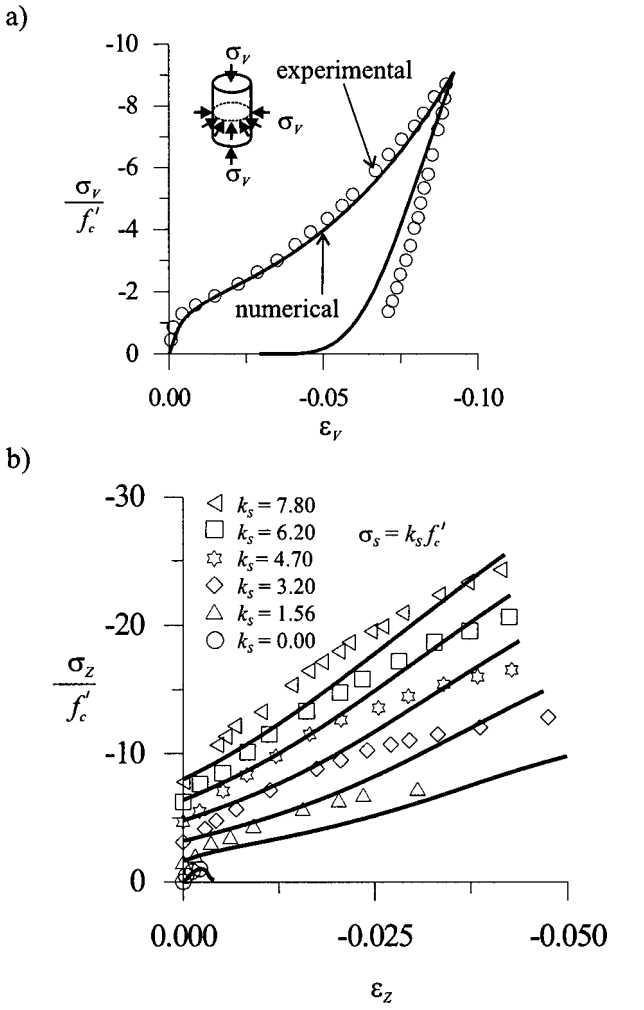

Fig. 8. (a) Hydrostatic compression and (b) triaxial compression response for various levels of confining pressure

lateral surface of cylindrical specimens a confining pressure equal to the longitudinal stress. The load is increased up to, approximately, ten times the compressive strength and after that the specimen is unloaded. The agreement between the computed response and the experimental data is very good. The behavior is initially elastic. For $\sigma \approx 1.5 f_c'$, the linearity is lost, because of densification due to compression crushing of the cement paste pores on the mesolevel, but the response remains hardening. If the load is increased further, the tangent modulus begins to increase, reaching eventually very high values, explained by the closing of pores. The computed tangential unloading stiffness is elastic at the beginning and tends to decrease to zero at complete unloading.

In the standard triaxial tests, concrete is subjected to mildly nonproportional loading. Cylindrical specimens are first subjected to hydrostatic pressure σ_S and then the axial stress is increased while the lateral confining stress is kept constant at σ_S. Fig. 8(b) compares the computed response to Balmer's (1949) experimental data by plotting the measured nominal stress–strain relation during the nonproportional loading path. The confining pressures corresponding to $\sigma_S / f_c' = 0$, 1.56, 3.2, 4.7, 6.2, and 7.8 are considered. The agreement between the computed curves and the experimental data points appears to be quite satisfactory.

Summary and Conclusions

The present two-part study develops a new lattice-type model for inelastic behavior and fracture of concrete, realistically simulating the essential features of the mesostructure of large aggregate particles embedded in cement mortar. The mechanical behavior is characterized by constitutive relations in terms of one normal and two shear components of the stresses and strains at the cross section of a particle-connecting strut corresponding to the contact layer between two adjacent particles. Formulation of this relation exploits analogy with the microplane model. The interfacial transition zone is assumed to act in series coupling with the bulk of matrix. The new model has several advantages over the existing models:

1. The same model (with the same parameters) can realistically simulate the inelastic triaxial behavior, strength limits, and postpeak response for both tension and compression. This elusive goal is achieved by virtue of the following features:
   a. The model is three-dimensional.
   b. The struts connecting the particle centers resist not only the axial force between the adjacent particles but also the shear forces resulting from the rotations of the adjacent particles.
   c. The shear resistance is achieved without introducing flexure-resistant moment-transmitting struts, which has been an artificiality of some previous models.
   d. The softening response of the connections depends on the lateral confining pressure that acts on the connecting strut.
   e. The shear and confinement effects in the struts are a necessary and advantageous substitute for an order-of-magnitude lattice refinement which would be needed on the level of mortar if the lattice were pin jointed.
2. The model can simulate all the essential known aspects of the tensile, compressive, and shear failure of concrete; the fracture behavior; postpeak softening and its localization; and the transitional size effect. [Although this has not been demonstrated, the model should in principle also be able to capture the vertex effect (Caner et al. 2002), and the size effect for failures at crack initiation.]
3. The mesostructure of large particles is generated randomly according to the prescribed particle size distribution. The procedure to do this is simple, thanks to the fact that the aggregate particles are not in contact. Delaunay triangulation is used to determine the particle connections and their cross-section areas.
4. An efficient explicit dynamic numerical algorithm is formulated, and the numerical stability restriction on the magnitude of the time step is derived.
5. The new model has been shown capable of simulating a broad range of experimental data for concrete, including:
   a. Correct elastic Poisson's ratio.
   b. Tensile strength equal to about 1/10 of the compressive strength.
   c. Realistic volume changes and lateral strains in uniaxial compression tests.
   d. Realistic biaxial failure envelope and biaxial strain softening.
   e. Hydrostatic pressure response, with the characteristic S-shaped curve of pressure versus volume change, hydrostatic unloading, and the fact that pure hydrostatic pressure never produces softening (this feature is missed by most continuum models for concrete).
   f. Triaxial response, including the stiffening of response with increasing lateral confining pressure.

g. Correct localized patterns as observed in compression testing, particularly the axial splitting when the platens are almost frictionless and formation of cones or pyramids under the platens when the friction is not minimized.
h. Realistic cyclic hysteretic loops for loading into the softening range, for both tension and compression, and approximate approach to the virgin softening curve after load cycles.
i. Correct cracking localization patterns in tensile failure of both unnotched and notched specimens.
j. Correct size effect in geometrically similar notched specimens, agreeing with Bažant's size effect law, and a realistic value of the initial fracture energy deduced from the size effect.

Acknowledgments

The work of two of the writers (G.C. and Z.P.B.) on both parts I and II of this study was partially supported under U.S. National Science Foundation Grant No. CMS-9732791 to Northwestern University. The work of two of the authors (G.C. and L.C.) was further partially supported under the European Commission ANCHR Project at Politecnico di Milano.

Appendix. Central Difference Algorithm Used

The time history is subdivided by times t_n $(n=1,2,...,N)$ in finite steps Δt. For the nth time increment, the matrix Eq. (1) is $\mathbf{M}\ddot{\mathbf{Q}}^n + \mathbf{C}\dot{\mathbf{Q}}^n + \mathbf{P}(\mathbf{Q}^n) = \mathbf{F}(t^n)$. The central difference approximations of the derivatives are (e.g., Underwood 1983) $\dot{\mathbf{Q}}^{n-1/2} = (-\mathbf{Q}^{n-1} + \mathbf{Q}^n)/\Delta t$, $\ddot{\mathbf{Q}}^n = (-\dot{\mathbf{Q}}^{n-1/2} + \dot{\mathbf{Q}}^{n+1/2})/\Delta t$. Also, denote $\dot{\mathbf{Q}}^n = (\dot{\mathbf{Q}}^{n-1/2} + \dot{\mathbf{Q}}^{n+1/2})/2$. Using these approximations, one gets from the foregoing matrix equation:

$$\dot{\mathbf{Q}}^{n+1/2} = (\mathbf{M}/\Delta t + \mathbf{C}/2)^{-1}[(\mathbf{M}/\Delta t + \mathbf{C}/2)\dot{\mathbf{Q}}^{n-1/2} + (\mathbf{P}^n - \mathbf{F}^n)] \tag{8}$$

and

$$\mathbf{Q}^{n+1} = \mathbf{Q}^n + \Delta t \dot{\mathbf{Q}}^{n+1/2} \tag{9}$$

where $\mathbf{P}^n = \mathbf{P}(t^n)$ and $\mathbf{F}^n = \mathbf{F}(t^n)$. To preserve the memory storage features of the central difference integrator, the mass and the damping matrices must be diagonal. If we assume $\mathbf{C} = C\mathbf{M}$ and denote $v = C\Delta t/2$, we set from Eq. (8) $\dot{\mathbf{Q}}^{n+1/2} = [(1-v)\dot{\mathbf{Q}}^{n-1/2} + \Delta t \mathbf{M}^{-1}(\mathbf{P}^n - \mathbf{F}^n)]/(1+v)$.

If $\mathbf{M}$ is diagonal, we can also write the previous expression component by component, obtaining

$$\dot{Q}_i^{n+1/2} = [(1-v)\dot{Q}_i^{n-1/2} + \Delta t(P_i^n - F_i^n)/M_i]/(1+v) \tag{10}$$

The expressions (10) cannot be used at the beginning of the integration because the velocity is not known at $t^{-1/2}$ but only at t^0. The initial conditions are $\mathbf{Q}^0 = \mathbf{0}$ and $\dot{\mathbf{Q}}^0 = \mathbf{0}$. The latter gives $\dot{\mathbf{Q}}^{-1/2} = -\dot{\mathbf{Q}}^{1/2}$ and so $\dot{\mathbf{Q}}^{1/2} = \Delta t \mathbf{M}^{-1}(\mathbf{P}^0 - \mathbf{F}^0)/2$, and component by component we get $\dot{Q}_i^{1/2} = \Delta t(P_i^0 - F_i^0)/(2M_i)$.

The last expressions and Eq. (10) are valid for unconstrained degrees of freedom, at which the static boundary conditions (loads F_i^n) can be applied. When the kinematic boundary conditions are prescribed, the velocities are known and the aforementioned expressions must be used to compute the reactions at the boundaries. We have $\dot{Q}_i^{n+1/2} = \dot{\delta}_i^{n+1/2} = \dot{\delta}_i(t^{n+1/2})$, $\dot{Q}_i^{n-1/2} = \dot{\delta}_i^{n-1/2} = \dot{\delta}_i(t^{n-1/2})$, and so $\dot{\delta}_i^{n+1/2} = [(1-v)\dot{\delta}_i^{n-1/2} + \Delta t(P_i^n - R_i^n)/M_i]/(1+v)$, from which $R_i^n = P_i^n - [(1-v)M_i\dot{\delta}_i^{n-1/2} + (1+v)M_i\dot{\delta}_i^{n+1/2}]/\Delta t$. For $n=0$ we have $\dot{\delta}_i^{-1/2} = -\dot{\delta}_i^{1/2}$, $\mathbf{Q}^0 = \mathbf{0}$, $P_i^0 = 0$, and $R_i^0 = 2M_i\dot{\delta}_i^{1/2}/\Delta t$.

In the present computations, the boundary conditions have been applied "softly" by prescribing a velocity field at all lattice nodes in an imagined layer of material artificially added to the specimen surfaces (in on-going work extending this paper, this procedure is now superseded by a complete simulation of the specimen surfaces).

References

Balmer, G. G. (1949). "Shearing strength of concrete under high triaxial stress—Computation of Mohr's envelope as a curve." *Struct. Res. Lab. Report No. SP-23*, U.S. Dept. of the Interior and Bureau of Reclamation, Denver.

Bažant, Z. P. (1984). "Size effect in blunt fracture: Concrete, rock, metal." *J. Eng. Mech.*, 110(4), 518–535.

Bažant, Z. P. (2002a). "Concrete fracture models: Testing and practice." *Eng. Fract. Mech.*, 69, 165–205.

Bažant, Z. P. (2002b). *Scaling of structural strength*, Hermes-Penton, London.

Bažant, Z. P., and Becq-Giraudon, E. (2001). "Estimation of fracture energy from basic characteristics of concrete." *Fracture mechanics of concrete (Proc., FraMCoS-4 Int. Conf., Paris)*, R. de Borst, J. Mazars, G. Pijaudier-Cabot, and J. G. M. van Mier, eds., Lisse: Swets & Zeiftlinger, A. A. Balkema, Rotterdam, The Netherlands, 491–495.

Bažant, Z. P., and Cedolin, L. (1991). *Stability of structures: Elastic, inelastic, fracture, and damage theories*, Oxford University Press, New York.

Bažant, Z. P., and Planas, J. (1998). *Fracture and size effect in concrete and other quasibrittle materials*, CRC Press, Boca Raton, Fla.

Bažant, Z. P., Tabarra, M. R., Kazemi, T., and Pijaudier-Cabot, G. (1990). "Random particle model for fracture of aggregate or fiber composites." *J. Eng. Mech.*, 116(8), 1686–1705.

Bažant, Z. P., and Yu, Q. (2002). "Choice of standard fracture test for concrete and its statistical evaluation. *Int. J. Fracture*, 118(4), Dec., 303–337.

Belytschko, T., Liu, W. K., and Moran, B. (2000). *Nonlinear finite elements for continua and structures*, Wiley, Chichester, U.K.

Broek, D. (1988). *The practical use of fracture mechanics*, Kluwer Academic, Dordrecht.

Caner, F. C., Bažant, Z. P., and Červenka, J. (2002). "Vertex effect in strain-softening concrete at rotating principal axes." *J. Eng. Mech.*, 128(1), 24–33.

Cedolin, L., Dei Poli, S., and Iori, I. (1987). "Tensile behavior of concrete." *J. Eng. Mech.*, 113(3), 431–449.

Cusatis, G., Bažant, Z. P., and Cedolin, L. (2003). "Confinement-shear lattice model for concrete damage in tension and compression: I. Theory." *J. Eng. Mech.*, 129(12), 1439–1448.

Green, S. J., and Swanson, S. R. (1973). "Static constitutive relation for concrete." *Rep. No. AFWL-TR-72-2*, Air Force Weapons Lab., Albuquerque, N.M.

Hognestad, E., Hanse, N. W., and McHenry, D. (1955). "Concrete stress distribution in ultimate strength design." *ACI J.*, 52(4), 455–480.

Kupfer, H., Hildsorf, H. K., and Rüsch, H. (1969). "Behavior of concrete under biaxial stresses." *J. Am. Concr. Inst.*, 66, 656–666.

Mihashi, H., and Izumi, M. (1977). "Stochastic theory for concrete fracture." *Cem. Concr. Res.*, 7, 411–422.

Planas, J., Elices, M., and Guinea, G. V. (1992). "Measurement of the fracture energy using three-point bend tests: Part 2—Influence of bulk energy dissipation." *Mater. Struct.*, 25, 305–312.

Reinhardt, H. W., and Cornellissen, H. A. W. (1984). "Postpeak cyclic

behavior of concrete in uniaxial tensile and alternating tensile and compressive loading.'' *Cem. Concr. Res.*, 14, 263–270.
Sinha, B. P., Gerstle, K. H., and Tulin, L. G. (1964). ''Stress–strain relations for concrete under cyclic loading.'' *J. Am. Concr. Inst.*, 62, 195–210.
Underwood, P. (1983). ''Dynamic relaxation.'' *Computational methods for transient analysis 5*, T. J. R. Hughes and T. B. Belytschko, eds., Elsevier Science, Amsterdam, The Netherlands, 245–265.
van Mier, J. G. M. (1986). ''Multiaxial strain-softening of concrete. Part I: Fracture.'' *Mater. Struct.*, 19, 179–190.
van Mier, J. G. M., Shah, S. P., Arnaud, M., Balayssac, J. P., Bascoul, A., Choi, S., Dasenbrock, D., Ferrara, G., French, C., Gobbi, M. E., Karihaloo, B. L., Köning, G., Kotsovos, M. D., Labuz, J., Lange-Kornbak, D., Markeset, G., Pavlovic, M. N., Simsch, G., Thienel, K.-C., Turatsinze, A., Ulmer, M., van Geel, H. J. G. M., van Vliet, M. R. A., and Zissopoulos, D. (1997). ''Strain-softening of concrete in uniaxial compression. Report of the Round Robin Test carried out by RILEM TC 148-SSC.'' *Mater. Struct.*, 30, 195–209.
van Vliet, M. R. A., and van Mier, J. G. M. (1995). ''Softening behavior of concrete under uniaxial compression.'' *Fracture mechanics of concrete structures* (FraMCoS-2, Zürich), F. H. Wittman, ed., Aedificatio, Freiburg, Germany, 383–396.
Vonk, R. A. (1992). ''Softening of concrete loaded in compression.'' PhD Thesis, Eindhoven Univ. of Technology, Eindhoven, The Netherlands.